Title
Characterization of spectral-domain OCT with autocorrelation interference response for axial resolution performance.

Journal
Optics Express, 26(6)

ISSN
1094-4087

Authors
Moon, Sucbei
Qu, Yueqiao
Chen, Zhongping

Publication Date
2018-03-19

DOI
10.1364/oe.26.007253

Peer reviewed

Research Article | Vol. 26, No. 6 | 19 Mar 2018 | OPTICS EXPRESS 7253
Optics EXPRESS

Characterization of spectral-domain OCT with autocorrelation interference response for axial resolution performance

SUCBEI MOON,[1,2] YUEQIAO QU,[1,3] AND ZHONGPING CHEN[1,3,*]

[1]*Beckman Laser Institute, Univ. of California, Irvine; 1002 Health Sciences, Irvine, CA 92617, USA*
[2]*Department of Physics, Kookmin Univ.; 77 Jeonneung-ro, Seoul 02707, South Korea*
[3]*Department of Biomedical Engineering, Univ. of California, Irvine; 5200 Engineering Hall, Irvine, CA 92697, USA*
**z2chen@uci.edu*

Abstract: We present a class of novel system characterization methods for spectral-domain optical coherence tomography (SD-OCT) particularly on getting optimized axial resolution performance. Our schemes uniquely utilize the autocorrelation interference response, also known as the self-interference product, which is generated by the optical fields from the imaging sample in automatic interferences. In our methods, an autocorrelation-inducing calibration sample was prepared which was made by sandwiching glass plates. OCT images of the calibration sample were captured by an SD-OCT system under testing. And the image data were processed to find various system characteristics based on the unique properties of autocorrelation interferograms, free of dispersion- and polarization-involved modulations. First, we could analyze the sampling characteristic of the SD-OCT's spectrometer for spectral calibration that enables accurate linear-*k* resampling of detected spectral fringes. Second, we could obtain the systematic polarization properties for quantifying their impact on the achieved axial resolutions. We found that our methods based on the autocorrelation response provide an easy way of self-characterization and self-validation that is useful in optimizing and maintaining axial resolution performances. It was found very attractive that a variety of system characteristics can be obtained in a single-shot measurement without any increased system complexity.

OCIS codes: (110.4500) Optical coherence tomography; (170.4500) Optical coherence tomography; (110.2650) Fringe analysis; (300.6190) Spectrometers.

References and links

1. R. K. Wang and Z. Ma, "A practical approach to eliminate autocorrelation artefacts for volume-rate spectral domain optical coherence tomography," Phys. Med. Biol. **51**(12), 3231–3239 (2006).
2. B. J. Davis, T. S. Ralston, D. L. Marks, S. A. Boppart, and P. S. Carney, "Autocorrelation artifacts in optical coherence tomography and interferometric synthetic aperture microscopy," Opt. Lett. **32**(11), 1441–1443 (2007).
3. M. G. Hyeon, H.-J. Kim, B.-M. Kim, and T. J. Eom, "Spectral domain optical coherence tomography with balanced detection using single line-scan camera and optical delay line," Opt. Express **23**(18), 23079–23091 (2015).
4. S. Moon and D. Y. Kim, "Normalization detection scheme for high-speed optical frequency-domain imaging and reflectometry," Opt. Express **15**(23), 15129–15146 (2007).
5. M. Szkulmowski, A. Wojtkowski, T. Bajraszewski, I. Gorczynska, P. Targowski, W. Wasilewski, A. Kowalczyk, and C. Radzewicz, "Quality improvement for high resolution in vivo images by spectral domain optical coherence tomography with supercontinuum source," Opt. Commun. **246**(4-6), 569–578 (2005).
6. A. K. Gaigalas, L. Wang, H. J. He, and P. DeRose, "Procedures for wavelength calibration and spectral response correction of CCD array spectrometers," J. Res. Natl. Inst. Stand. Technol. **114**(4), 215–228 (2009).
7. M. Jeon, J. Kim, U. Jung, C. Lee, W. Jung, and S. A. Boppart, "Full-range k-domain linearization in spectral-domain optical coherence tomography," Appl. Opt. **50**(8), 1158–1163 (2011).
8. T. J. Eom, Y. C. Ahn, C. S. Kim, and Z. Chen, "Calibration and characterization protocol for spectral-domain optical coherence tomography using fiber Bragg gratings," J. Biomed. Opt. **16**(3), 030501 (2011).
9. M. Mujat, B. H. Park, B. Cense, T. C. Chen, and J. F. de Boer, "Autocalibration of spectral-domain optical coherence tomography spectrometers for in vivo quantitative retinal nerve fiber layer birefringence determination," J. Biomed. Opt. **12**(4), 041205 (2007).

#318229 https://doi.org/10.1364/OE.26.007253
Journal © 2018 Received 21 Dec 2017; revised 26 Feb 2018; accepted 27 Feb 2018; published 12 Mar 2018

Optics EXPRESS

10. X. Liu, M. Balicki, R. H. Taylor, and J. U. Kang, "Towards automatic calibration of Fourier-Domain OCT for robot-assisted vitreoretinal surgery," Opt. Express **18**(23), 24331–24343 (2010).
11. J. H. Kim, J. H. Han, and J. Jeong, "Accurate wavelength calibration method for spectrometer using low coherence interferometry," J. Lightwave Technol. **33**(16), 3413–3418 (2015).
12. K. Wang and Z. H. Ding, "Spectral calibration in spectral domain optical coherence tomography," Chin. Opt. Lett. **6**(12), 902–904 (2008).
13. D. J. Faber and T. G. van Leeuwen, "Doppler calibration method for Spectral Domain OCT spectrometers," J. Biophotonics **2**(6-7), 407–415 (2009).
14. M. Szkulmowski, S. Tamborski, and M. Wojtkowski, "Spectrometer calibration for spectroscopic Fourier domain optical coherence tomography," Biomed. Opt. Express **7**(12), 5042–5054 (2016).
15. B. Park, M. C. Pierce, B. Cense, S.-H. Yun, M. Mujat, G. Tearney, B. Bouma, and J. de Boer, "Real-time fiber-based multi-functional spectral-domain optical coherence tomography at 1.3 μm," Opt. Express **13**(11), 3931–3944 (2005).
16. Y. Chen, Z. Li, N. Nan, Y. Bu, X. Wang, L. Pan, and X. Wang, "Automatic spectral calibration for polarization-sensitive optical coherence tomography," Opt. Express **25**(20), 23605–23618 (2017).
17. Z. Hu and A. M. Rollins, "Fourier domain optical coherence tomography with a linear-in-wavenumber spectrometer," Opt. Lett. **32**(24), 3525–3527 (2007).
18. E. Z. Zhang, W.-Y. Oh, M. L. Villiger, L. Chen, B. E. Bouma, and B. J. Vakoc, "Numerical compensation of system polarization mode dispersion in polarization-sensitive optical coherence tomography," Opt. Express **21**(1), 1163–1180 (2013).
19. M. Wojtkowski, V. Srinivasan, T. Ko, J. Fujimoto, A. Kowalczyk, and J. Duker, "Ultrahigh-resolution, high-speed, Fourier domain optical coherence tomography and methods for dispersion compensation," Opt. Express **12**(11), 2404–2422 (2004).
20. S. Moon, S.-W. Lee, and Z. Chen, "Reference spectrum extraction and fixed-pattern noise removal in optical coherence tomography," Opt. Express **18**(24), 24395–24404 (2010).
21. J. M. Lerner, "Imaging spectrometer fundamentals for researchers in the biosciences-A tutorial," Cytometry A **69**(8), 712–734 (2006).

1. Introduction

Optical coherence tomography (OCT) takes depth-resolved reflectance images on imaging samples from their interference products. In the analytic terminology, the OCT interferometer is an optical analyzer that finds the correlations of the optical fields involved. The correlations appear in the acquired spectral interferograms, *i.e.*, fringed signals given in optical frequency domain, which can be acquired by a spectral acquisition means in Fourier-domain OCT (FD-OCT). The reflectance profiles in depth, called OCT A-lines, are reconstructed from frequency-domain interference responses through a fringe analysis technique of the Fourier transform. The OCT interferometer is basically intended to obtain the mutual correlation of the field coming from the sample and the reference field fed by the system. This image-forming process is called *cross-correlation* (XC) which suggests the interference of the sample field to the reference. Meanwhile, in a whole package, the interferogram unavoidably includes the correlation of the sample field to itself. Referred to as *autocorrelation* (AC), a fringed interference response is generated through the automatic interferences of the sample field's components that come from different parts of the imaging sample [1,2].

The presence of the AC-involved interference response is obviously an unpleasant feature and has been regarded as a characteristic artifact of the FD-OCT modality. It often results in annoying ghost images in the form of faint images followed by the desired XC-produced real ones. They may become quite visible when the sample has a strong reflecting plane which provides a secondary reference field. This issue arises more often with spectral-domain OCT (SD-OCT) systems which are based on spectrometric detectors mostly without balanced photodetection capabilities [2–4]. In reduced intensities, however, the swept-source OCT (SS-OCT) systems may produce noticeable AC-involved responses due to the limited common-mode rejection of balanced detectors [4].

Although the AC response is of no use in OCT imaging, it can be utilized for system characterization and optimization. Its characteristic uniqueness comes from the nature of generation involved solely with the sample fields with no regard to the OCT system. Note that the axial resolutions of the XC-generating OCT images are largely influenced by the systematic factors of dispersion and polarization. Because of their combined effects, it

Optics EXPRESS

requires elaborate investigations to accurately characterize those properties. In contrast, those systematic factors do not disturb the AC-producing signals. If an AC-inducing sample is free of dispersion and polarization-involved properties, it will be able to provide an uncontaminated form of spectral interferograms. It can be smartly utilized as a norm of the interference responses that can correct the faulty system in normalizing the characteristics.

In this report, we present useful methods of characterization and optimization for an SD-OCT system based on the AC-involved effects. For this purpose, we made a calibration sample that brings strong AC interference responses from its well-defined multiple reflections. It simply consisted of two glass plates separated by an air gap. Its OCT images were naturally rich in AC-involved contents which could be distinguished and extracted by using a signal processing technique. As an outstanding advantageous feature, our methods only demand a set of OCT A-line data with no added parts or reconfigurations of the system for testing. Even from a single A-line, it is possible to obtain various characteristics with help of *a priori* knowledge of the sample's structure.

First, we analyzed the OCT spectrometer's sampling characteristics from the AC response. Our calibration sample provided an AC interferogram which was a simple sinusoidal function of frequency under no phase disturbances. From the ideal fringe form, the spectrometer could be calibrated to correct the spectral OCT signals to be later acquired. Note that a grating-based spectrometer used widely as a signal acquisition means for an SD-OCT system does not detect the signals in a correctly registered manner in frequency or wavenumber (denoted by k, hereafter) [5–16]. It needs an accurate calibration for so-called linear-k resampling. This problem can be alleviated by an improved design of linear-in-k spectrometers [17] but with a limited accuracy. The signal correction of k-domain resampling has paramount importance in obtaining fine spatial resolutions and phase measurement accuracies [9,15,16]. The AC response could be used for this as an excellent reference signal form for its unusual property.

Second, we took advantage of the AC response's unique polarization property. Polarization rarely plays a role in the AC generation while the XC-involved processes are likely affected by the differences in the polarization states caused by different optical paths of the sample and reference fields. The XC responses are often complicated by the presence of systematic polarization mode dispersion (PMD) which may give frequency-dependent polarization state mismatches between the two fields. Because of the barely controllable nature of optical fibers in polarization, accurate validation of resolution performances is difficult unless built in free-space optics or equipped with a polarimetric detection capability [18]. These difficulties in validation consequently hinder getting an optimized resolution performance. In this study, the polarization effects in forming the XC-involved OCT images were quantitatively analyzed through signal normalizations with the measured AC response. It could help us comprehend the polarization-related characteristics of the system as well as other systematic flaws that might make impacts on the resolution performance.

This report is structured as follows: In Section 2, a theoretical overview will be presented on OCT signal formation as well as the basic elements of our signal processing techniques. In Section 3, the methods used in our experiment and data processing work will be described. The experimental results will be shown together for multiple stages of our system characterizations. Section 4 will give in-depth analyses on the benefits and the limiting factors of our methods as well as a comprehensive comparison to the competing techniques developed earlier by others.

2. Theory

A. Formation of AC interference response

In this section, we are going to use the complex notation of optical waves, described in either electric or magnetic field, and take the squared absolute of a field for optical intensity. The OCT signal is generated by combining the optical field from the sample, E_s, and the reference

Optics EXPRESS

field, E_R, in mutual interferences. Through square-law detection, the intensity of the interfered field signal, denoted by I, is measured by a photodetector as

$$I = \left|E_R + E_S\right|^2 = I_R + I_S + \left(E_R^* E_S + E_R E_S^*\right) \tag{1}$$

where I_R and I_S are intensities of the reference and sample fields, respectively. Here, the complex conjugate and the absolute of field E is denoted by E^* and $|E|$, respectively. In a particular case of interest where the OCT imaging sample contains two distinct reflection points indexed by n and m, the sample field consists of two components, E_n and E_m, with their corresponding intensities, I_n and I_m, respectively. Then, the measured intensity turns out to be

$$I = I_R + I_S + 2\mathbf{Re}\left\{E_R^* E_n + E_R^* E_m + E_n^* E_m\right\} \tag{2}$$

where $\mathbf{Re}\{\cdots\}$ is to take the real part of a complex. Realization of each correlation term makes a cosine function with a phase function for its argument. Equation (2) can be rewritten as

$$I = I_R + I_S + A_n \cos\phi_n + A_m \cos\phi_m + A_{nm} \cos\Delta\phi \tag{3}$$

where ϕ_n and ϕ_m are the phase functions of E_n and E_m, respectively, measured in respect to that of the reference field while $\Delta\phi$ is the difference of ϕ_n to ϕ_m. Expressing the polarization-involved effect in a simplified way, the amplitudes of the correlation terms in Eq. (3); A_n, A_m and A_{nm}; are respectively expressed by

$$A_n = 2\gamma\sqrt{I_R I_n} \tag{4a}$$

$$A_m = 2\gamma\sqrt{I_R I_m} \tag{4b}$$

$$A_{nm} = 2\sqrt{I_n I_m} \tag{4c}$$

where γ is the polarization match factor given in the range of 0 to 1. It quantifies the polarization-involved efficiency in forming the XC interference. Notice that Eq. (4) assume the space between the two sample points is optically isotropic and the two sample fields are consequently in the same polarization states.

The phase function of ϕ_n or ϕ_m is a relative optical group delay or optical path-length difference (OPD) which makes up the axial-distance domain of z. The OPD may have frequency dependence related to chromatic dispersion [19]. But $\Delta\phi$ is still the difference of those two phase functions so that the common-path dispersion completely vanishes. The remaining dispersion in $\Delta\phi$ also becomes zero when the dispersion of the in-between space is negligibly low. After all, $\Delta\phi$ can make a perfectly linear function of $k = 2\pi/\lambda$ for wavelength λ. It is simply given by $\Delta\phi(k) = \Delta z \cdot k$ for the roundtrip OPD distance equal to Δz. This signal component given by the last term of Eq. (3) can be used as a calibration ruler for the linear-k sampling as will be described in the following section.

This feature of the AC interference response can be generalized. Note that for an optimized resolution performance, it is important to keep the sample field in balance with the reference field in terms of spectrum shape, chromatic dispersion and polarization state. Any mismatches would result in degradation of achievable axial resolutions involved with the XC products. There are a number of systematic factors that may cause imbalance because the fields of E_s and E_R reach the detector through different signal paths in the OCT system. On the contrary, the AC response is given directly by the imaging sample under better control. The sample itself provides an auxiliary interferometer for the AC generation which can easily be made free of imbalances.

Optics EXPRESS

B. Signal component extraction

In general, interferogram signals come in a mixed from. To be utilized in characterization, it requires a processing means which extracts a component of interest from the acquired composite signal. Any of the correlation terms given in Eq. (3) can be distinguished in the Fourier transform of $I(k)$ in the case where each occupies a different band in z. A signal processing of z-domain spatial filtering gives an amplitude function in a complex form by

$$\tilde{A}_\eta(k) = 2\cdot\mathbf{F}^{-1}\left\{\mathbf{F}\left\{I(k)\right\}\cdot\Pi_\eta(z)\right\} \tag{5}$$

for its absolutized function to become $A_\eta(k)$ where η is an index of the signal component in extraction; n, m or nm. Notice that η is a doublet for an AC-involved signal component. Here, $\mathbf{F}\{\cdots\}$ and $\mathbf{F}^{-1}\{\cdots\}$ denote the Fourier transform (FT) and the inverse Fourier transform (IFT), respectively. The kernel of the filter, Π_η, is a rectangular function of a proper z-domain selection. It gives unity within the passband of selection and zero in the rejection as illustrated in Fig. 1. Only taking the positive or negative part of z in selection, the Hilbert transform is embedded in the extraction process of Eq. (5). The resultant analytic function of a complex form can be used in detecting the envelope (A_η) or the phase (ϕ_n, ϕ_m or $\Delta\phi$) of the extracted signal component. It is worth noting Eq. (5) is only valid when the signal components of different origins are non-overlapping in z, separated apart with spatially confined point-spread functions (PSFs). This condition can be practically satisfied for a certain sample where the involved OPDs exceed a few hundreds of microns.

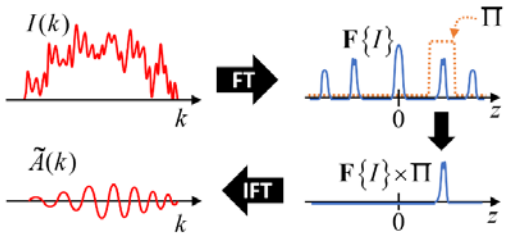

Fig. 1. Illustrative description of the extraction process for a fringe component by using a spatial filter of Π (z).

Reconstructed by Eq. (5), the amplitude functions of A_n, A_m and A_{nm} give a simple way of getting γ from Eq. (4). It is obtained by

$$\gamma(k) = \sqrt{\frac{A_n A_m}{2I_R A_{nm}}} \tag{6}$$

from the spatially filtered fringes along with the separately measured reference spectrum of I_R. Because a low level of PMD produces a moderate frequency dependence on γ in most systems, it can be smoothened by a curve fitting or a low-pass filter to cope with a limited signal-to-noise ratio (SNR). Note that being divided by the square root of A_{nm} on the right side of Eq. (6) may magnify the noise contents in obtaining a good accuracy for γ. Meanwhile, the extracted fringe amplitude function also gives a simple way of finding an individual sample field. The measured functions of γ and I_R give a conversion relation as

$$I_\eta(k) = \left(\frac{1}{4\gamma^2 I_R}\right)\cdot A_\eta^2 = \Gamma(k)\cdot A_\eta^2(k) \tag{7}$$

where η is the index of a sample field in retrieval. Here, the sample intensity spectrum is reconstructed from the squared fringe amplitude function multiplied by a conversion factor of

Optics EXPRESS

$\Gamma(k)$ which is determined by γ and I_R. Originally extracted by Eq. (6), use of a smoothened function of γ in Eq. (7) may help this retrieval for accuracy.

3. Method and result

A. Calibration sample and SD-OCT system

In our experiment, an AC-inducing calibration sample was made of top and bottom glass plates placed parallel to each other. The top plate was a 0.17-mm thick microscope cover glass while the bottom was a much thicker glass substrate. They were separated by keeping the space between them empty in the air as illustrated in Fig. 2(a). The thickness of the air gap, d, was 1.14 mm. For the three glass surfaces from the top, the planes were indexed by 0, 1 and 2. And their reflected fields were denoted by E_0, E_1 and E_2, respectively. The last plane underneath was not considered because it was surely located beyond the OCT imaging range. Meanwhile, by placing a beam blocker above the glass plates, a part of the glass plane's area was shaded from the OCT light illumination. The beam blocker's surface was largely tilted for its specular reflection not to return back to the probing optics. The OCT image of the calibration sample was taken so that an image frame included a completely black area at a side which contained virtually no sample fields. This part of the image was used for reference spectrum measurements in our OCT imaging.

The SD-OCT system used in this study was of a classic design with a wide operation bandwidth. In its home-made spectrometer based on a diffraction grating, a silicon line CCD of 2,048 pixels was utilized. Its light source provided a wideband spectrum centered at 850 nm in wavelength. For fine axial resolutions, the acquisition range of the spectrometer was taken wide, ranging 750 nm through 940 nm. The system had a fiber-optically implemented Michelson interferometer with two polarization controllers. At the sample arm, an objective lens and galvo beam scanners were equipped for imaging. OCT images were obtained with an objective lens and galvo beam scanners. The dispersion was not well matched between the sample and reference arms. The amount of imbalanced dispersion was estimated to be that of a 25-mm glass path. It must be emphasized that throughout our experiment, the OCT image acquisitions were conducted by keeping the system unchanged as in usual OCT imaging modes. Thus, our performance characterizations were on the system *in situ*, not in a certain special configuration for testing.

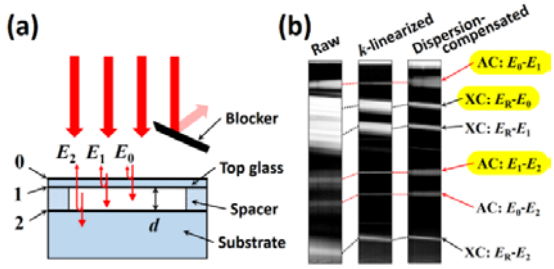

Fig. 2. AC-producing calibration sample made of glass plates used in our SD-OCT system characterizations (a) and its partial OCT images (b).

The acquired OCT signal was processed step by step. The signal was resampled with the spectrometer calibration information which was obtained by the method we developed in this research. A numerical dispersion compensation was applied afterwards. Each processing gave a characteristic image result. Figure 2(b) shows partial OCT images obtained in the processing steps. In all cases, each line running horizontally was produced by an interference product of AC or XC. The left side of Fig. 2(b) shows the partial OCT image obtained from the raw signal's direct Fourier transforms. It exhibits all blurry lines because of the improper signal sampling and the systematic dispersion imbalance. In the middle of Fig. 2(b), the

Optics EXPRESS

partial image shows that *k*-linear resampling sharpened the AC lines best. On the right side, the dispersion-compensated image exhibits sharp XC-involved lines with re-blurred AC lines. The origin of each horizontal line can be recognized with ease by the known structure of our calibration sample. Due to a slight tilt of our calibration sample in respect to the scan axis, the XC lines appear to be noticeably sloped while the AC lines remain perfectly horizontal. Those features helped in finding the types of interference products.

B. Calibration of spectrometer for linear-k resampling

Among six fringe components of the OCT image, the AC-involved interferogram of the E_1-to-E_2 correlation was used in our spectrometer calibration for its dispersion-free property because this signal component was produced by the OPD of the air gap. In obtaining a pure form of the AC fringe from the acquired composite signal, the spectral interferogram of I_{AC} in a complex analytic form could be obtained by

$$I_{AC}(p) \equiv \frac{1}{2} A_{12}(p) \cdot e^{+i\Delta\phi(p)} = \mathbf{F}^{-1}\left\{\mathbf{F}\left\{I(p)\right\} \cdot \Pi_{AC}(z')\right\} \tag{8}$$

where p is the detector's pixel index, z' is the Fourier-conjugate domain of p, and Π_{AC} is a rectangular function of selecting the E_1-E_2 correlation product in the positive side of z'. This formula is an adaptation of Eq. (5) for p and z', which correspond to k and z, respectively. The filtering operation does not have to be performed in the z domain in an exact sense. The nonlinearity of p to k was so moderate that the spatial filter acting in z' made little difference. Based on its origin, the AC response of I_{AC} must give a sinusoidal fringe of a constant period in the domain of k. But a nonlinear relation of p to k gives a phase modulation observed in the fringe arranged in p. The signal resampling is to correct this misalignment of data points so that the resampled I_{AC} exhibits no phase modulation.

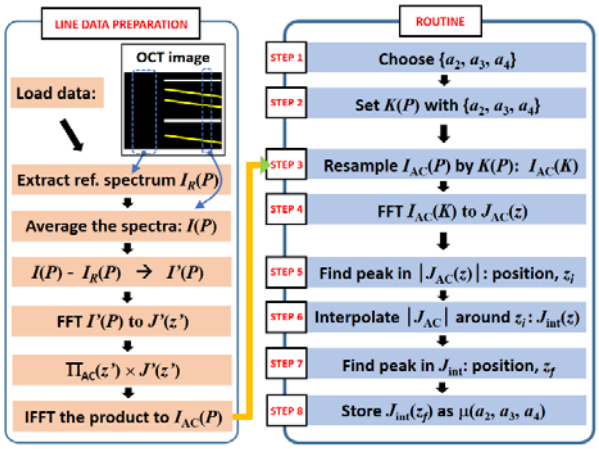

Fig. 3. Computational procedure of finding a peak amplitude of an AC response for a given set of parameters, $\{a_2, a_3, a_4\}$, from a spectral signal of $I(P)$ acquired with the calibration sample.

For mathematical simplicity, we define a normalized coordinate of P used for the detector pixel coordinate. Here, its range is 0 through 1 in a direct proportion to p. As well, we define a normalized wavenumber coordinate of K reduced from k. We chose $K = 0$ for $P = 0$ and $K = 1$ for $P = 1$ for simplicity. Owing to the inversion symmetry and the translation symmetry in FD-OCT imaging, the signal point of $K = 0$ could be selected freely to be either the highest or the lowest point of k. Calibration of the spectrometer is, then, to find a proper map for P-to-K conversion. A polynomial curve fit provides a simple function for that. A fourth-order polynomial function is expressed by

Optics EXPRESS

$$K = \left(1 - a_2 - a_3 - a_4\right)P + a_2P^2 + a_3P^3 + a_4P^4 \tag{9}$$

with three active coefficients of a_2, a_3 and a_4. Use of the normalized coordinates automatically determines the zeroth-order and the first-order coefficients to be $a_0 = 0$ and $a_1 = 1\text{-}a_2\text{-}a_3\text{-}a_4$ from the given boundary conditions. In most cases of practice with Eq. (9), the third-order fit will suffice in taking $a_4 = 0$. Finding a set of best matching coefficients is an optimization of problems with the running parameters of the polynomial coefficients. A measure of merit or suitability for the parameters can be the peak amplitude found in the FT of the AC fringe. For this, the peak amplitude is taken from the signal resampled by Eq. (9) with coefficients of $\{a_2, a_3, a_4\}$. In the complete absence of phase errors, the AC response will produce the highest possible peak when those parameters are fully optimized.

Optimization of the polynomial coefficients can be accomplished by various methods. We used the least efficient but the most straightforward way of the global search algorithm that finds the full merit function of parameters in a widest possible range. Figure 3 shows the process routine of finding a peak value, μ, to be used for a merit evaluator for a chosen combination of coefficients. Before running the routine, a spectral A-line data set, $I'(P)$, was prepared from an OCT image of our calibration sample by, first, averaging ten A-line signals for a better SNR and, second, subtracting the reference spectrum to remove the fixed-pattern noise [20]. The reference was separately obtained from the black area of the image for this. In the third, the E_1-E_2 AC component was extracted to make $I_{AC}(P)$ by operation of the fast Fourier transform (FFT) and the inverse FFT (IFFT) as given in Eq. (8). Therein, the filter function of Π_{AC} was manually set up for its passband in z' to cover a virtually full range of the E_1-E_2 AC signal component, still avoiding possible collisions with neighboring signal bands.

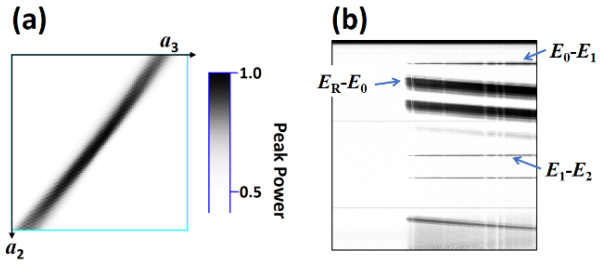

Fig. 4. Map of peak powers, μ^2, in two-dimensional space of parameters (a) and the OCT image of our calibration sample at the best parameters of the spectrometer calibration (b).

Fed to the main routine, the data set of the spectral interferogram was resampled by a polynomial function of $K(P)$ given by the coefficients under examination. It was performed by a spline interpolation of the data point conversion from P to K with the total number of data points unchanged. After the FFT was processed on the resampled data, the peak of amplitudes was searched in its absolutized A-line. The accuracy of this initial peak finding was hindered by sparseness of the data points. To alleviate this problem, a second spline interpolation of sub-pixel magnification was applied to the A-line data in the vicinity of the initially found peak position. A better peak value was finally obtained this way with enhanced precision. This computational routine was repeated for a number of coefficient combinations to make the full map of peaks, denoted by $\mu(a_2, a_3, a_4)$. The task of the optimization work was completed by finding $\{a_2, a_3, a_4\}$ at the maximum of μ which best fit the actual P-K relation.

In our experiment, the optimization work was performed with the 3rd-order and the 4th-order fits for a comparison. Figure 4 shows the result obtained in the 3rd-order optimization case: graphical representation of $\mu(a_2, a_3)$ in 2D space (a) and the OCT image obtained with the best of $\{a_2, a_3\}$ (b). The OCT image of Fig. 4(b) is displayed in inverted brightness for better visual clarity. As seen in Fig. 4(a), the distribution of peak powers gives a

Optics EXPRESS

monotonically peaked function of a_2 and a_3. This property suggests that it is possible to use more efficient optimization techniques with no concern for multiple local maxima. Meanwhile, based on the known physical thickness of the air gap that was involved with the E_1-E_2 AC response, the full OCT imaging range was calibrated to be 2.07 mm for the axial extent.

C. Dispersion compensation

The axial blurs observed at the XC-involved lines in Fig. 4(b) suggest the presence of systematic dispersion imbalance in a large quantity. To fully validate the imaging performance, the OCT images needed a numerical dispersion compensation [19]. This subject is out of the main scope of this report but needs to be addressed here for full understanding of our signal processing procedures. The dispersion compensation can be performed by applying a frequency-dependent phase that effectively neutralizes the phase errors caused by the dispersion mismatch. The final OCT A-line, denoted by $J(z)$, is obtained by

$$J(z) = \mathbf{F}\left\{ I(k) \cdot e^{-i\Phi(k)} \right\} \tag{10}$$

in a complex form where $\Phi(k)$ is the dispersion-induced phase deviation to be compensated. In a popular third-order polynomial expansion, the phase function gives

$$\Phi(K) = \left(-b_2 - \frac{3}{4} b_3 \right) K + b_2 K^2 + b_3 K^3 \tag{11}$$

with two dispersion coefficients of b_2 and b_3. Here, the first-order coefficient (b_1) is determined so that the derivative of $\Phi(K)$ equals zero at the midpoint of K = 1/2. It approximately corrects the unwanted group delay produced by Φ.

In a similar way to the parameter optimization for our spectrometer calibration, the best combination of $\{b_2, b_3\}$ could be searched by using a merit evaluator of the peak power obtained from the OCT data. In our calibration sample, the top glass was very thin and gave only a negligible dispersion. The response of interest could be, then, any of the three XC-involved responses. We used the E_R-E_0 XC response in optimizing the dispersion coefficients. By using a global search algorithm with the same OCT data set as the spectrometer calibration, the best coefficient combination was found which maximized the peak amplitude of the point response. Because of the added phase shifts of -Φ, the AC response became no more of a linear phase function of k and spatially spread in z at the optimal dispersion compensation.

D. Resolution performance validation

The width of spatial spreads for a point response given in $|\mathbf{F}\{I\}|$, known as the resolution of a PSF, is affected by the deviation of its phase from a linear function of k. Such an undesired phase error can be caused by imperfect system optimizations or other error sources. To estimate the overall degree of phase linearity, a figure of merit (FOM) on the resolution performance can be taken by

$$\mathrm{FOM}_\eta = \frac{\delta z}{\delta z_0} = \frac{\mathbf{W}\left[\left| \mathbf{F}\left\{ \tilde{A}_\eta(k) \right\} \right| \right]}{\mathbf{W}\left[\left| \mathbf{F}\left\{ A_\eta(k) \right\} \right| \right]} \tag{12}$$

for a certain PSF indexed by η, where $\mathbf{W}[\cdots]$ is to take the width of the peak found in the A-line. Here, the PSF is a z-domain response of either XC or AC interference in a context. In the case of an AC-produced PSF, η is a doublet index with two numbers that respectively refer to the field components in AC interference. In accordance to the convention of the axial

Optics EXPRESS

resolutions, we measured the full width at half maximum (FWHM) in A-line amplitude, as called the 6-dB resolution. The FOM is, thus, a ratio of the measured PSF width, δz, to its transform limit, δz_0, which can be obtained by ignoring the phase contribution. When the FOM approaches unity, a transform-limited resolution is achieved.

The FOM analysis was made with the acquired AC responses in order to validate the overall accuracy of the spectrometer calibration. The response under testing was the E_0-E_1 AC for its doublet index η to be 01. Note that the spectrometer calibration was conducted with the other AC response of the E_1-E_2 interference product as explained earlier. For the E_0-E_1 AC in the FOM analysis, the internal dispersion of the thin top glass was neglected. Two different image data sets before the numerical dispersion compensation applied were utilized. The cases of the 3rd-order and 4th-order polynomial optimizations were compared to each other in this analysis. Table 1 summaries the analysis results which suggest nearly transform-limited point spreads in all the cases. The 3rd-order polynomial seemed more practical for its reduced computational complexity. For OCT data processing described hereafter, the 3rd-order polynomial optimization was used unless mentioned otherwise.

Table 1. FOM analysis of the spectrometer calibration

Optimization mode	3rd-order fit		4th-order fit	
Measured resolution (δz)	3.56 μm	3.51 μm	3.67 μm	3.63 μm
Resolution limit (δz_0)	3.44 μm	3.47 μm	3.43 μm	3.46 μm
FOM_{01} ($\delta z/\delta z_0$)	**1.03**	**1.01**	**1.07**	**1.05**

Table 2. FOM analysis of the axial resolution performance

Type of PSF	E_R-E_0 XC		E_R-E_1 XC	
Axial position (z)	0.46 mm	0.70 mm	0.68 mm	0.92 mm
Measured resolution (δz)	4.31 μm	4.77 μm	4.77 μm	5.45 μm
Resolution limit (δz_0)	4.09 μm	4.64 μm	4.58 μm	5.33 μm
$FOM_{0/1}$ ($\delta z/\delta z_0$)	**1.05**	**1.03**	**1.04**	**1.02**

After the spectrometer calibration was validated, the FOM analysis was performed with the dispersion-compensated OCT image data sets. It evaluated the overall accuracy of the whole signal processing work. The XC responses of E_R-E_0 and E_R-E_1 in two different images were used for this. The analysis result is shown in Table 2. In all cases, the FOMs were well below 1.1 which demonstrates nearly transform-limited resolutions and suggests our system optimization methods are all successful. Figure 5 shows the images of a rabbit's cornea sample obtained after spectrometer calibration and dispersion characterization. Here, the reference spectrum was obtained from the intra-frame image data by using a median-line extraction technique [20]. The final image clearly demonstrates the success of the proposed technique that largely improves the image quality and axial resolutions.

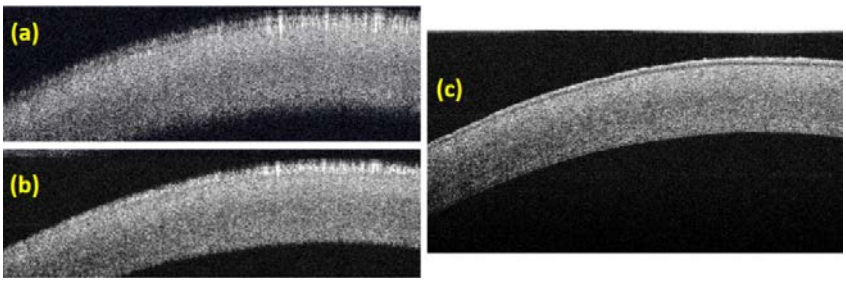

Fig. 5. OCT images of a rabbit's cornea, *ex vivo*, from the raw data (a), the linear-*k* resampled data (b), and the dispersion-compensated linear-*k* resampled data (c).

Optics EXPRESS

E. Polarization match factor and sample spectra

The formula of Eq. (5) provided a means of extracting the spectral shapes of the correlation signal components. From the image data, each could be distinguished through FFT, band selection and IFFT. Then, we could use those componential signals for system characterizations. In measuring the polarization match factor of γ, amplitude functions of A_0, A_1 and A_{01} were respectively extracted. For a combination of the AC and XC responses with $n = 0$ and $m = 1$, γ was calculated by Eq. (6). In addition, the spectra of the sample fields were calculated by using Eq. (7). Figure 6 shows the polarization match factor (a) and the sample fields' intensity spectra (b) retrieved this way.

The presence of a systematic PMD was clear from the polarization match factor depicted in Fig. 6(a) that gave a sine-like function of normalized k. In our SD-OCT system, a significant PMD was brought by fiber coils, mostly from the two polarization controllers. Each had three pedals of fiber rounds that could induce a retardation of ~1 wave (λ) or more in total. The round trips of two different arms could give ~4 waves or more in total. Considering the fractional bandwidth of 0.23 for the spectral detection range, roughly a cycle of relative polarization state variation might be produced through the spectral range. This estimation roughly agreed with the finding implied by Fig. 6(a). The information on γ provided a rule-of-thumb estimation on the polarization-involved impact on the obtainable resolution performance.

As seen in Fig. 6(b), the reconstructed spectra of the sample fields exhibited spectral features partially similar to those of the reference spectrum (I_R). But their spectra also exhibited considerable deviations from the reference spectrum. Especially, the sample spectra obtained at large OPDs, such as that of I_2 in Fig. 6(b), showed very different shapes losing most of the spectral characteristics coming from the source spectrum. The causes of those sample fields' spectral deviations will be discussed in the next section.

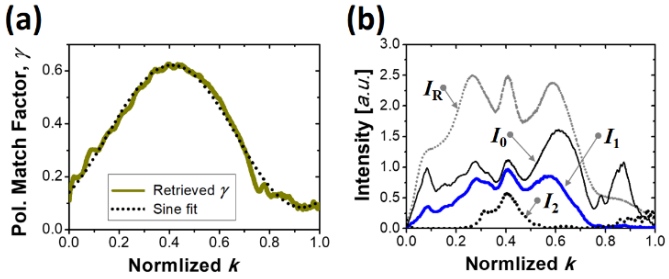

Fig. 6. Polarization match factor of γ (a) and the effective sample fields' spectra (b) retrieved from the filtered fringes of the XC and AC responses. The reference spectrum, I_R,was separately measured. Each trace has a different vertical scale in (b).

F. Effects of large PMD

The systematic PMD gives negative effects to the resolution performance as well as to the accuracy of the system optimization. Unlike the case of chromatic dispersions, PMD can be rarely compensated by using a numerical technique in a conventional OCT configuration because of its variable nature. We tested the robustness of our system optimization method under a high level of systematic PMD. A large amount of birefringence was introduced to the reference arm or the sample arm with a multi-order waveplate (WP) to simulate an OCT system with large PMD. The OCT image was captured for our calibration sample while the WP was in place. The additional PMD introduced by the WP produced an amplitude modulation of spectral fringes in the XC interferograms. We aligned the WP's rotational orientation for a large amplitude of the PMD-induced modulation. Meanwhile, it was found that the AC-involved interferograms were kept unchanged. We performed spectral calibration with the PMD-contaminated image data and found no noticeable difference. In addition, we

Optics EXPRESS

optimized the dispersion coefficients with the same data. As shown in Fig. 7(a), the result was almost the same as the one obtained with no WP. The slight difference in phase is thought to have partially originated from the dispersion of the WP placed in the system. Those results proved that our system optimization methods are robust against large PMDs.

The polarization match factor of γ was retrieved from the image data obtained with the WP in place. The calculation result is shown in Fig. 7(b) compared to the case of no WP. The trace of the sample field's relative polarization state with respect to that of the reference field's determines the plot of γ in normalized k. At $\gamma = 0$ where the fringe amplitude becomes zero, they pass through orthogonal polarization states. The relative polarization trace must have made a series of rotations in the Poincaré sphere introduced by the WP. The trace of Fig. 7(b) with the WP in place suggests that it passed points of orthogonal states by a nearly periodical manner in k. According to the manufacturer's data of the WP, it produces a relative retardation of ~2 waves over the spectral measurement range. A roundtrip doubled the amount and could make a rotation of ~4 turns in the Poincaré sphere that takes a spectral period of rotation to be $\delta K = 1/4$. The actual period observed in Fig. 7(b) was a little lower than 1/5 for δK. The PMD of the fibers could give approximately one more turn in the same rotational direction. In the other aspect, the overall shape of γ in normalized k resembled an absolutized sine function but with duller peaks than those of a sine function. The polarization match factor follows the inner product of the two polarization states. It would be a cosine function of k if the trace passed both the points of $\gamma = 0$ and $\gamma = 1$ in a period. The duller peaks of γ in our observation could be explained by the fact that the peak amplitude did not reach $\gamma = 1$. All those features seemed to match well with the expected polarization-involved characteristic. Again, this demonstrates that the retrieved γ function can give useful information on the systematic PMD in an SD-OCT system.

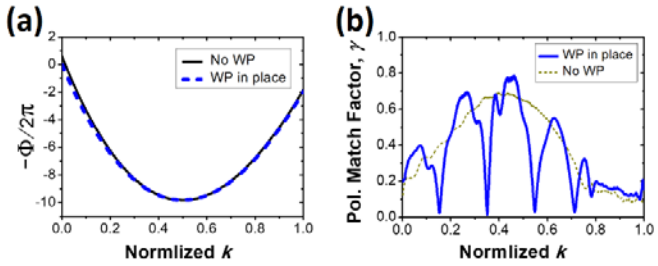

Fig. 7. Dispersion-compensative phase function with a multi-order WP placed in the reference arm (a) and the plot of the polarization match factor γ as a function of normalized k (b), compared to no WP in place.

4. Discussion

A. Spectrometer calibration

On the spectrometer calibration for the SD-OCT system, several useful schemes have been proposed so far. As a simple estimation scheme, the spectral characteristic can be obtained from the geometrical parameters of the spectrometer's optical design [5] but with limited precisions. In a classic approach, a calibration light source can be utilized which is based on a krypton lamp [6], a tunable filter [7], fiber Bragg gratings [8], *etc.* Whatever makes natural or artificial spectral signatures, if predictable, can be used for this. For conveniently making a calibration light source, M. Mujat *et al*. proposed a very simple scheme in which a thin glass plate is inserted at the output of the source [9]. Like an AC response in our method, their source spectrum provides a spectral fringe uniformly spanned in k which can be used for a k-domain calibration ruler. An obvious disadvantage those source-based approaches have in common comes from the need for specialized optical elements. Even in the conceptually

Optics EXPRESS

simple method of Mujat *et al.*, a pair of collimators need to be installed after the light source for placing a glass plate in the beam path.

It is no surprise that an OCT spectrometer can be calibrated very easily without a specialized source if the dispersion-involved effect is neglected in the system. That is the case of common-path OCT configurations [10] or OCT systems operating at the 1.3 μm band of low fiber dispersions with well-balanced arms [11]. Then, a mirror reflection itself gives a spectral fringe of *k*-domain sinusoid in its XC response. However, in the cases of non-negligible dispersion mismatches, a calibration scheme must cope with dispersion-induced chirps that reside in the PSFs. In a notably simple manner, K. Wang *et al.* solved this complication by taking two different PSFs using a sample mirror in precision translation [12]. In their method, equal contribution of the dispersion imbalance to the two PSFs was subtracted in their retrieved phase functions. However, its nature of double-shot measurements can hinder getting guaranteed accuracy. Changes in systematic polarizations or spectrally uneven back-coupling efficiencies might affect the calibration result. In a similar approach, a calibration scheme can utilize the Doppler frequency shifts produced by controlled mirror motions which are independent of the systematic dispersion mismatches [13,14]. This method can be interpreted as a dynamic variant of the double measurement scheme of K. Wang *et al.'s.* Those calibration methods can be suited for SD-OCT systems of different properties in different environments of calibration work.

Compared to the calibration schemes previously proposed, our spectral calibration method based on an AC-inducing calibration sample gives several superior features. As a versatile technique, it can be utilized for OCT systems of large dispersion and PMD mismatches. Due to the nature of the single-shot measurement, it is not vulnerable to an unstable measurement environment. It provides excellent usability involved with in-service calibrations. After the initial calibration, an occasional variation of the optical geometry, *e.g.*, in replacement of a component, may bring the necessity of recalibration. Our method provides a convenient way of spectrometer recalibration. It requires neither complication of the system nor the operator's access to the internal structure for readjustment. Our calibration method is easily performed in a normal imaging mode by simply taking an OCT image shot of the calibration sample.

In seeking the optimal mode of operation, our spectrometer calibration method has a couple of technical issues that need further discussion. The first one is on the signal processing algorithm used in finding the *P*-*K* conversion map. From the *k*-domain sinusoid extracted from the AC response, one can reconstruct its phase function directly through the Hilbert transform while we took an iterative optimization technique in our experiment. In a conceptually equivalent alternative to the phase function retrieval, the zero-crossing points of the filtered AC fringe can be directly used for points of signal resampling. In principle, all of those computational techniques may give the same result. Nevertheless, they may have different properties in terms of implementation complexity and operational robustness against the measurement noise. The phase function retrieval has an advantage in its conceptual and computational simplicity [12]. The phase retrieval can be processed faster in computation than the iterative counterpart. However, a direct use of the retrieved phase function is subject to random phase errors, especially when the signal's low SNR is concerned [14]. Taking a curve fit can be a method of choice under these circumstances. This is supported by the fact that the actual *P*-*K* map follows a slowly varying function that is determined by a simple optical geometry of the OCT spectrometer [5].

We tested the curve fitting of the phase function which was retrieved directly from the filtered AC response. The phase function was obtained by taking the angle of the complex I_{AC} function which was obtained by Eq. (8). The unwrapped phase function was taken as *K* after being normalized. It was fitted to a polynomial function afterwards by a least-square method. We found the resolution performance obtained this way was a bit inferior to our iterative processing. While our iterative optimization gave the FOM well below 1.1 as explained in Table 1, the FOM obtained from the direct phase retrieval was all over 1.1 depending on the

Optics EXPRESS

maximum polynomial order in the fitting. The main cause of the excessive errors was found to be involved with the phase unwrapping operation. Discontinuities in phase running were occasionally produced as a consequence of erroneous phase unwraps. Note that the accuracy of the phase retrieval is naturally limited by various noise sources. They include deterministic errors introduced by the finite bandwidth of the filtered fringe. As a matter of chance, small errors can occasionally be magnified to considerable errors of 2π radians in the phase unwrapping process. Its impact on the fitting result may depend on the mode of the polynomial function fit. If the maximum order of the polynomial was set relatively low, the abrupt phase jump would induce misfits over a wide range of k. In the opposite case that the order was set too high, its effect could be localized but would be more vulnerable to random phase noise. Besides the problem of unwrapping errors, the curve fitting with the retrieved phase may take inappropriate weightings on the phase data. The fringe spectrum has decreasing intensities at the side in low SNRs. The phase information coming from such untrusted data points has equal contribution in the fitting. After all, a curve fitting with the retrieved phase function is less robust against the local error sources.

The second technical issue on our spectrometer calibration scheme is about the choice of the merit evaluator. It is one of the characteristic elements of an iterative optimization technique. We took the peak amplitude of the AC-involved PSF for measuring the merit of a given set of parameters. However, the spatial width of the peak (δz) could be taken for the merit metric [14]. For experimental comparison, we ran the same optimization procedures in selecting the 6-dB width for the merit evaluator. We found this gave virtually the same result. It is worth noting that the width-based evaluator has an inherent risk of false maxima. In extreme cases where the parameters are far from optimal points, a large chirp of the spectral fringe may produce split peaks of individually narrow widths in z. Then, the optimization can be fooled by such a partial peak. The peak amplitude evaluator does not have such a risk and can optimize in stable operations.

The technical discussions given above on the optimization algorithm for our spectrometer calibration can all be repeated for numerical dispersion compensation. From an XC point response, one can retrieve the dispersion-induced phase function of $\Phi(k)$ and can directly derive the dispersion coefficients from it. Nonetheless, it seems more advantageous to use a search-based iterative optimization algorithm with a peak-amplitude merit evaluator.

B. Resolution performance validation

In the conventional OCT imaging, validation of the axial resolution performance has been usually conducted by comparing the measured resolution to the transform limit. This limit was estimated by the FT of the source's spectrum or alternatively the reference spectrum. Achieving a transform-limited resolution has meant that the OCT system obtains a best resolution performance that is achievable from the given source spectrum. This is a validation made on the overall resolution performance and does not specifically tell how much a certain physical or signal-processing element affects the obtained final resolutions. If the overall resolution performance did not meet the transform limit, one would have no other way except to investigate every part of the system. In this study, we found that an AC response contains rich contents on various aspects of the system's resolution performance. Specific performances of the image signal processes could be validated in a variety.

We developed two types of FOM validations with Eq. (12) as given in the previous section. The FOM on the AC-involved PSF was measured from the resampled data set before the dispersion compensation was applied. It solely quantified the accuracy of the spectrometer calibration. Meanwhile, the FOM on the XC-involved PSF measured with the final data set quantified the overall accuracy of those two processes as a whole. If the dispersion compensation was not successful, the XC-involved FOM would be noticeably worse than the AC-involved FOM. In this way, the FOM analysis provides self-validation and automatic checkups useful in system diagnosis which can be helpful guides for further investigations.

Optics EXPRESS

From the reference spectrum's FT in our system, the systematical transform-limited resolution was estimated to be 3.25 μm. The actually achieved resolutions were considerably worse than this, as listed in Table 2, depending on the position of a PSF and other factors. The best of the obtained resolutions was 4.31 μm. One of the possible causes responsible for this resolution degradation is the imperfect polarization matching involved with the systematic PMD as discussed with Fig. 6(a). Taking the Fourier transform with the polarization match factor expressed by $\mathbf{F\{}I_R\cdot\gamma\,(k)\mathbf{\}}$, the transform limit under the given γ was found to be 4.23 μm. It matched well with the best of the measured values, 4.31 μm. The best FOM taking γ into account was 1.02, reasonably low to be called transform-limited. This suggested that the polarization-involved effect was the major factor of resolution degradations in our current system.

In summary, four different levels of transform limits have been presented in this report. They are the resolutions of the point responses evaluated in (i) FT of the reference spectrum, (ii) FT of the reference spectrum weighted by γ, (iii) FT of the AC-involved fringe resampled in k, and (iv) FT of the AC fringe resampled and dispersion-compensated. A combination of FOM analyses with those four types of transform limits will provide a useful tool kit for system diagnosis in getting the best of axial resolution performances. This is a unique feature that our AC response-based measurement can provide.

C. Impact of finite spectral resolutions

Originally fed from the light source, the spectrum of a sample field is determined by its spectral transfer characteristics. It is a whole product of transmission efficiencies in k given by all the optical paths and the reflectivity at the sample. In our experiment, the sample spectra retrieved from the AC response, as in Fig. 6(b), suggested that the sample fields experienced uneven spectral transfers. The retrieved spectra differed considerably from the reference spectrum and even from each other. Including the non-uniform transmission at the fiber coupler, the probing optics of the sample arm might produce significant spectral unevenness. One should notice that the chromatic aberration and diffractions of the focusing optics could differentiate the spectral components when the sample fields were coupled back to the fiber in a confocal geometry. A tilt of the reflection planes could also contribute in conjunction with the wavelength-dependent processes. By direct sample spectrum measurements performed with a sample mirror while blocking the reference arm, we confirmed that a significant variation occurs to sample spectra in a manner quite sensitive to the mirror position. This partially explained the spectral variation of the sample fields given in Fig. 6(b).

Nevertheless, optical transfer characteristics could not explain all the features of the sample spectra, particularly the ones obtained at far regions of z. Those wavelength-selective effects were likely to give slowly varying functions of k in transfer. In contrast, it was repeatedly observed that a sample spectrum of a farther point got narrower in bandwidth. As the OPD approached the end of the imaging range, this effect of *bandwidth collapsing* got more apparent. For instance, in the case of I_2 in Fig. 6(b), only a narrow spectral band centered at $K = 0.4$ remained in the retrieved sample spectrum. Considering its sharp cut-offs at both sides, this effect cannot be explained by spectrally uneven recoupling efficiencies.

It is natural that the accuracy of our spectral analysis is affected by spectral detection means. One must be aware of possible impacts made by a real-world spectrometer which mostly exhibits considerable signal loss [21]. Such a partial signal loss is not thought to critically affect our spectrometer calibration as long as the acquired signal contains a strong enough AC-involved fringe. But the retrieved spectral information on the polarization match factor and the sample field spectra can be notably distorted as a consequence of non-constant fringe sensitivities. First of all, the photoelectronic photon-to-electron conversion in a photon detector lays a responsivity curve of k on a measured spectrum. But it applies to all the acquired spectra in common. Involved with a finite spectral resolution, however, detection

Optics EXPRESS

sensitivities of fine spectral features vary widely. A fundamentally limiting factor is found in the non-point but areal property of the pixel elements in a spectrometer camera. Intra-pixel integration of detected photons gives an inherent spatial low-pass filter. In an approximated sense, its effect can be described by a magnitude transfer function (MTF) of a sinc function. The effective bandwidth of the MTF is inversely proportional to the relative pixel size. An optical MTF governed by the aberrations of the focusing optics must also be taken into account in a multiplication manner. Those signal blurring effects can hinder fine features of spectral interferograms from being efficiently detected by the camera. Because of those inevitable signal losses, fringe components extracted from far regions of z are presumably inaccurate and need careful interpretation in our analysis.

In reality, the spectral resolution of a spectrometer is not uniformly determined over the detection range. It is a consequence of the spectrometer's imperfection in optical design. Just like other lens-based imaging systems, the beam focusing lens of a spectrometer, if uncorrected in aberrations, must exhibit various spatial spreads that affect the spectral resolutions. The best resolution is usually obtained in the paraxial region around the lens axis. Oblique rays are more prone to focal power spreads through comma, astigmatism and Petzval field curvature. The schematic of Fig. 8(a) illustrates the effect of Petzval field curvature on the pixel-dependent spectral resolutions. The image plane of the lens is curved while the sensor plane of the camera is flat. The focus is matched only at the center but deviates from the sensor at both sides under the illustrated circumstances. The fringe visibility is lost at off-focused regions for a very fine fringe. Other types of aberrations may also contribute to this effect. The loss of fine features at the out-of-center regions expected from a badly corrected lens can explain the bandwidth collapsing phenomena we observed in the retrieved sample spectra. We experimentally found that slightly readjusting the sensor plane in axial position gave a spectrally uneven change to very fine spectral fringes. It strongly suggested the presence of field curvature. This problem may be alleviated by improving the optical design of the spectrometer. This will surely help the SD-OCT system maintain its transform-limited resolutions over a wide axial imaging range.

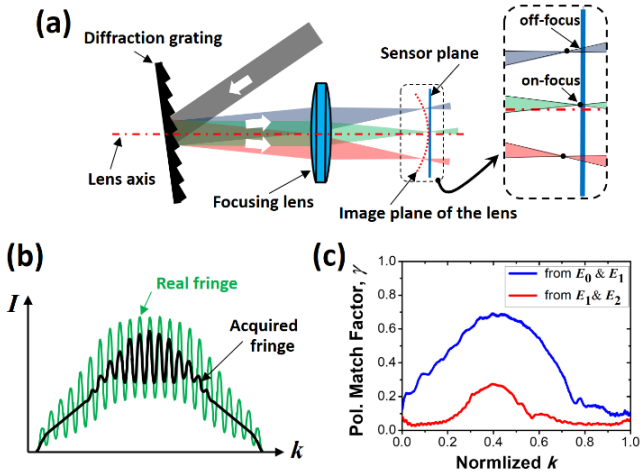

Fig. 8. Schematic of the camera-equipped spectrometer with a large field curvature (a), an exemplary fringe acquisition in the presence of position-dependent optical aberrations (b), and the polarization match factors retrieved from different combinations of the acquired correlation responses (c).

The finite spectral resolution of the OCT spectrometer is definitely a limiting factor of our system characterization methods. Retrieval of the sample spectrum cannot always reproduce the actual sample spectrum with exact amplitude and shape. It rather estimates an effective portion of the sample spectrum in producing detectable interference products so that it can be

Optics EXPRESS

called *effective sample spectrum*. Retrieval of γ by Eq. (6) is affected by the effective sample spectra. Figure 8(c) shows the very effect of OPD-dependent effective sample spectra on the retrieved polarization match factor. From the same A-line data set, two different γ's were retrieved. One was from an E_0-E_1 AC response, actually the same plot as that of Fig. 6(a). The other one was from an E_1-E_2 AC response. For the former, all the signal components used in calculation were extracted in a close region of z<0.7 mm with little loss of fringe visibilities. For the latter, the extracted A_2 was centered at z = 1.7 mm, near the limit of z, where bandwidth collapsing seriously matters. It must have decreased the amplitude and collapsed the bandwidth for the E_1-E_2-involved γ as seen in Fig. 8(c).

Despite the limitation of our spectral retrieval technique, it can be useful in system characterization if used carefully. For a reliable analysis result, the fringe components involved need to be extracted from the close side of z where the signal loss can be neglected. Notably, considerable differences found in a pair of separately retrieved γ's, if any, can be used for an indicator of effective signal losses. Particularly, notable disagreement in shape must be a useful signature. It indicates unequal spectral resolutions involved with optical aberrations in the spectrometer's optics. It should be noted that the right positioning of the detector camera requires precision work in the spectrometer alignment. The indicator of z-dependent γ functions can be used in monitoring the spectrometer's resolution performance for getting optimal alignments. Because our calibration sample always provides two different AC responses, this analysis can also be performed from a single-shot measurement.

5. Conclusion

In this report, we introduced a group of powerful measurement and characterization techniques which are useful in fully utilizing the potential resolution powers of the SD-OCT system. Our measurement could be simply completed by taking an OCT image on the calibration sample. The following signal processes of fringe extractions enabled us to obtain multiple interferograms captured simultaneously in a shot. We could utilize an AC interferogram sinusoid for a spectrometer calibration by taking advantage of the guaranteed k-domain periodic feature. As well, we could obtain the polarization match factor and the effective sample fields' spectra by normalizing the extracted interferograms to each other. Through our experiments, we found that our methods based on the AC interference response could successfully characterize the SD-OCT system with excellent measurement simplicity. All the characterization work could be performed with a single-shot data set acquired in a normal OCT imaging mode with no added complexity to the system. We believe that our system characterization methods will be very useful not only in system production but also in routine performance checkups, including occasional recalibration or readjustment to maintain the best axial resolutions of the system.

Funding

National Institutes of Health (NIH) (R01HL-125084, R01HL-127271, R01EY-026091, P41EB-015890), and the Air Force Office of Scientific Research (FA9550-17-1-0193).